2010

Surface Roughness Effect on Ultracold Neutron Interaction With a Wall and Implications for Computer Simulations

Albert Steyerl
University of Rhode Island, asteyerl@uri.edu

Surendra S. Malik
University of Rhode Island, smalik@uri.edu

See next page for additional authors

Citation/Publisher Attribution

Steyerl, A., Malik, S. S., Desai A. M., & Kaufman, C. (2010). Surface Roughness Effect on Ultracold Neutron Interaction With a Wall and Implications for Computer Simulations. *Physical Review C. 81*(5), 055505. doi: 10.1103/PhysRevC.81.055505
Available at: http://dx.doi.org/10.1103/PhysRevC.81.055505

Surface roughness effect on ultracold neutron interaction with a wall and implications for computer simulations

A. Steyerl,* S. S. Malik, A. M. Desai, and C. Kaufman
Department of Physics, University of Rhode Island, Kingston, Rhode Island 02881, USA
(Received 19 November 2009; published 28 May 2010)

We review the diffuse scattering and the loss coefficient in ultracold neutron reflection from slightly rough surfaces, report a surprising reduction in loss coefficient due to roughness, and discuss the possibility of transition from quantum treatment to ray optics. The results are used in a computer simulation of neutron storage in a recent neutron lifetime experiment that reported a large discrepancy of neutron lifetime with the current particle data value. Our partial reanalysis suggests the possibility of systematic effects that were not included in this publication.

DOI: 10.1103/PhysRevC.81.055505 PACS number(s): 28.20.−v, 14.20.Dh, 21.10.Tg

I. INTRODUCTION

The scattering and absorption of cold and ultracold neutrons (UCN) at slightly rough surfaces resembles the roughness problem in light and x-ray optics [1]. Surface roughness induces losses in neutron guide tubes and affects the behavior of a UCN gas in a trap. We investigate especially the relation between a realistic account of roughness in computer simulations of UCN storage and a reliable data interpretation with respect to the neutron lifetime. The issue has gained added importance since a new UCN storage-based lifetime value 6 standard deviation away from the world average value [2] was published in 2005 [3].

Most theoretical analyses of diffuse cold and ultracold neutron scattering at surfaces with small roughness (e.g., [4–7]) are based on first-order perturbation theory. A possible extension to macroscopic ray optics was presented in Ref. [4]. Carrying the analysis to second-order perturbation theory, Ignatovich [7] derived the roughness effect on the loss coefficient for reflection at a slightly absorbing wall material. The analysis was complex, and the result has, apparently, not been numerically evaluated and applied so far. We used a more direct approach, verified and quantified the result of Ref. [7], and in the process obtained a derivation of the "Debye-Waller factor" (describing the attenuation of the specular beam due to roughness) that is consistent with standard expressions but requires fewer assumptions about the roughness characteristics. This appears important since in practical cases very little is known about the roughness parameters of a given surface. Finally, we address the question to what extent a transition to a macroscopic picture is possible.

II. CORRELATION FUNCTIONS DESCRIBING A ROUGH SURFACE

Small irregular deviations of a slightly rough surface from the plane geometry are usually described by a height-height correlation

$$f(\boldsymbol{\delta}) = \lim_{A\to\infty} \frac{1}{A} \int_A \xi(\boldsymbol{\rho})\xi(\boldsymbol{\rho}+\boldsymbol{\delta})\, d^2\boldsymbol{\rho}, \tag{1}$$

where $\xi(\boldsymbol{\rho})$ is the random elevation at point $\boldsymbol{\rho} = (x, y)$ of the plane surface above its average $z = 0$. A is the illuminated surface area and $\boldsymbol{\delta}$ is the displacement vector between two points. Among common models [4–6], we will concentrate on a Gaussian correlation for solid surfaces with mean-square roughness $b^2 = \langle \xi^2 \rangle$:

$$f_G(\boldsymbol{\delta}) = f_G(\delta) = b^2 \exp[-\delta^2/(2w^2)] \tag{2}$$

and a "K_0 model" [5] for liquids and possibly glasses retaining characteristics of a liquid below the glass transition:

$$f_K(\boldsymbol{\delta}) = f_K(\delta) = b^2 \frac{K_0\{[(\delta^2+\delta_0^2)/(2w^2)]^{1/2}\}}{K_0[\delta_0/(w\sqrt{2})]} \tag{3}$$

The latter form contains the modified Bessel function K_0 and has been proposed in Ref. [6] as a modification of a liquid model with logarithmic short-range divergence [5] [which would imply a divergence of $g(\delta)$, see below] to account for smoothing due to surface tension. Smoothing is achieved by applying a short-range cutoff, δ_0, in addition to the long-range cutoff w that is used for both models. In Ref. [4,6] we have emphasized the importance of the slope-slope correlation for the surface gradient $\boldsymbol{\chi} = \nabla\xi(\boldsymbol{\rho})$:

$$g(\boldsymbol{\delta}) = g(\delta) = \lim_{A\to\infty} \frac{1}{A} \int_A \boldsymbol{\chi}(\boldsymbol{\rho}) \cdot \boldsymbol{\chi}(\boldsymbol{\rho}+\boldsymbol{\delta})\, d^2\boldsymbol{\rho} = -\nabla^2 f(\delta), \tag{4}$$

which is determined by $f(\delta)$ through the Laplace operator ∇^2. This can be verified using Gauss's divergence theorem. For the Gaussian model:

$$g_G(\delta) = \alpha_G^2 \left(1 - \frac{\delta^2}{2w^2}\right) \exp[-\delta^2/(2w^2)] \tag{5}$$

with mean-square slope $\alpha_G^2 = \langle \chi^2 \rangle = g(0) = 2b^2/w^2$. For the "$K_0$ model" [6]

$$g_K(\delta) = \alpha_K^2 \frac{P\{[(\delta^2+\delta_0^2)/(2w^2)]^{1/2}\}}{P[\delta_0/(w\sqrt{2})]} \tag{6}$$

with

$$P(\nu) = \frac{\delta_0^2/(2w^2)}{\nu^2} K_2(\nu) - K_0(\nu)$$

*asteyerl@mail.uri.edu

and

$$\alpha_K^2 = \frac{b^2}{w^2}\frac{K_1(t)}{tK_0(t)}.$$

To facilitate comparison with the Gaussian model we choose δ_0 such that for given b and w the mean-square slopes become identical: $\alpha_G^2 = \alpha_K^2 = \alpha^2$. This requires $t = \delta_0/(w\sqrt{2}) = 0.7709$, which is the solution of $K_2(t)/K_0(t) = 5$.

Fairly smooth surfaces with small α^2 are best characterized by $g(\delta)$. For surfaces with tips and sharp edges the curvature-curvature correlation function

$$h(\boldsymbol{\delta}) = h(\delta) = \lim_{A\to\infty}\frac{1}{A}\int_A \kappa(\boldsymbol{\rho})\kappa(\boldsymbol{\rho}+\boldsymbol{\delta})\,d^2\boldsymbol{\rho} = \frac{1}{4}\nabla^2\nabla^2 f(\delta) \tag{7}$$

may not be negligible, either. For $\alpha^2 \ll 1$ the mean surface curvature is given by $\kappa = \frac{1}{2}(\frac{\partial^2\xi}{\partial x^2} + \frac{\partial^2\xi}{\partial y^2}) = \frac{1}{2}\nabla^2\xi$ and represents the mean curvature in any two orthogonal in-plane directions x and y. The operations in (7) can be performed using the properties of Bessel functions. The results are given in Appendix A. The mean values are

$$\kappa_G^2 = h_G(0) = 2b^2/w^4 = \alpha^2/w^2$$

and

$$\kappa_K^2 = h_K(0) = 2.103\alpha^2/w^2$$

for $t = 0.7709$, as before.

We add a note related to calculations of "Debye-Waller factors" describing the decrease of specular intensity, for larger momentum transfer, due to destructive interference within the rough layer. These are based on probability distributions for height, $p(\xi)$, or slope, $p(\eta)$, etc., that require additional assumptions about surface properties. For instance, the commonly used Gaussian form $p(\xi) = b^{-1}(2\pi)^{-1/2}\exp[-\xi^2/(2b^2)]$, which is normalized and has second moment $\langle\xi^2\rangle = b^2$, is *not* implied by the Gaussian form of $f(\delta)$; only the second moment is common. While the correlations (4) and (7) and higher are unambiguously determined by $f(\delta)$ alone, all the higher moments for $p(\xi)$ constitute additional assumptions. For real surfaces even b and w are usually not well known. We show below that from $f(\delta)$ alone a Debye-Waller factor can be determined, but only up to order b^2, if the perturbation approach for the rough wall is carried to second order. Other assumptions usually made to derive "Debye-Waller factors" will also be discussed.

We will also point out that asymptotic aspects of roughness-induced scattering and absorption can be obtained from mean values (b^2, α^2, etc.) only, independently of the details of the models used (Gaussian or "K_0" or similar). Going to second-order perturbation is both necessary and sufficient for a full account of reflection and absorption up to quadratic terms (b^2). Higher perturbations are at least of order b^4 for symmetrical roughness where $f(\boldsymbol{\delta}) = f(-\boldsymbol{\delta})$.

III. PERTURBATION APPROACH TO UCN INTERACTION WITH A ROUGH WALL

As usual [4–6], a wall with micro-roughness may be divided into a volume V_0 with an ideally smooth wall at $z = 0$, and a thin roughness volume V_1 with partly positive and partly negative thickness $\xi(\boldsymbol{\rho})$, where $\langle\xi\rangle = 0$. For an incident plane wave $\psi_i(\mathbf{r}) = \exp(i\mathbf{k}_i\cdot\mathbf{r}) = \exp(-ikz\cos\theta_i)\exp(ikx\sin\theta_i)$ approaching the surface from the vacuum side ($z > 0$), the neutron wave function $\psi(\mathbf{r})$ may be split into the unperturbed part $\psi_0(\mathbf{r})$ for the plane surface and a small perturbation $\psi_1(\mathbf{r})$:

$$\psi(\mathbf{r}) = \psi_0(\mathbf{r}) + \psi_1(\mathbf{r}) \cong \psi_0(\mathbf{r}) + \psi_1^{(1)}(\mathbf{r}) + \psi_1^{(2)}(\mathbf{r}). \tag{8}$$

The first-order perturbation is obtained [4] as

$$\psi_1^{(1)}(\mathbf{r}) = -q_0\int G(\mathbf{r}|\mathbf{r}')\psi_0(\mathbf{r}')d^3\mathbf{r}', \tag{9}$$

where the scattering potential $q_0 = Na(1-i\eta) = k_c^2/4\pi = (k_{c0}^2/4\pi)(1-i\eta)$ is determined by Na, a mean value for the number N of atoms times their bound-atom scattering length a. The imaginary part given by $\eta = -Im(q_0)/Re(q_0)$ takes into account loss processes (nuclear capture, inelastic, and, except for UCN, incoherent-elastic scattering). η is small for wall materials of interest for UCN storage. k_{c0} denotes the critical wave number for total reflection at normal incidence on a flat wall of uniform scattering potential.

The Green's function $G(\mathbf{r}|\mathbf{r}')$ in (9) satisfies the equation

$$\nabla^2 G(\mathbf{r}|\mathbf{r}') + K^2(\mathbf{r})G(\mathbf{r}|\mathbf{r}') = -4\pi\delta(\mathbf{r}-\mathbf{r}'), \tag{10}$$

where $K(\mathbf{r})$ is the wave number: $K = k$ in vacuum and $K = (k^2 - k_c^2)^{1/2}$ within the medium. For negligible refraction, $G(\mathbf{r}|\mathbf{r}') = \exp(ik|\mathbf{r}-\mathbf{r}'|)/|\mathbf{r}-\mathbf{r}'|$. For the general expressions see Appendix B. Asymptotic expressions for $G(\boldsymbol{\rho}, z|\boldsymbol{\rho}', z')$ in the limit of large r have been used in Ref. [4].

This method can readily be extended to obtain the second- and higher-order perturbations. To obtain the $(n+1)^{th}$ order correction to $\psi_1(\mathbf{r})$ we insert $\psi_1^{(n)}(\mathbf{r})$ in the integral of (9), and below we will apply this method to extend roughness scattering to second order. Going to third or higher order would require correlations of higher than the second order.

Instead of the "distorted Green's function method" of Ref. [4] used here, an alternative distorted-wave Born approximation (DWBA) was used in Ref. [5]. In Ref. [6] it was shown that the two methods are equivalent, with one important caveat: A conventional "Born approximation" uses the far-field Green's function expansion to obtain the factor $\exp[i(\mathbf{k}-\mathbf{k}_i)\cdot\mathbf{r}']$ inside the integral. This gives an adequate description only in first order. Second-order calculations require also the near field of the Green's function, at $z \approx 0$, in the integral of (9) to obtain $\psi_1^{(1)}(\mathbf{r})$ at the rough surface. A variation of this method was used earlier in Ref. [7].

IV. GEOMETRY, BASICS, AND MAIN RESULTS

For a wave incident with a wave number k in the zx plane perpendicular to the wall at polar angle θ_i (measured from the wall normal), Fig. 1 shows projections of incident (i), reflected (r), and (elastically) scattered (s) wave vectors onto the xy

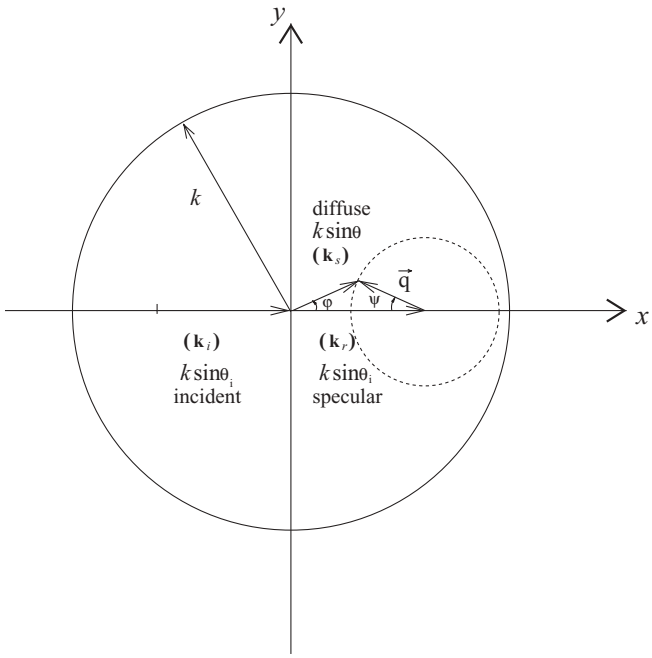

FIG. 1. For elastic wall interaction of UCN with wave number k we show the projections onto the surface plane of incident ($\mathbf{k}_i$), mirror-reflected ($\mathbf{k}_r$), and diffusely scattered ($\mathbf{k}_s$) wave vectors. The in-plane wave vector transfer $\mathbf{q}$ is the component of $\mathbf{k}_s - \mathbf{k}_r$ parallel to the surface. The vectors are bracketed to indicate projection onto the xy plane. For elastic scattering the end points of $\mathbf{q}$ are confined to the circle of radius k.

plane. The scattered beam at solid angle (θ, φ) is characterized by the in-plane momentum transfer parallel to the wall, $\mathbf{q} = (\mathbf{k}_s - \mathbf{k}_r)_{\text{par}}$, where

$$q = k\left[(\sin\theta - \sin\theta_i)^2 + 4\sin\theta\sin\theta_i\sin^2\frac{\varphi}{2}\right]^{1/2}. \tag{11}$$

Since we consider only elastic scattering, the end point of $\mathbf{q}$ is restricted to the area inside the circle with radius k. For the part of ψ containing the outgoing wave and the evanescent wave inside the medium we use the expansion

$$\psi_{\text{out}}(\mathbf{r}) = \psi_{0r}(\mathbf{r}) + \psi_1^{(1)}(\mathbf{r}) + \psi_1^{(2)}(\mathbf{r}), \tag{12}$$

where

$$\psi_{0r}(\mathbf{r}) = \begin{cases} R(\theta_i)\exp(ikz\cos\theta_i)\exp(ikx\sin\theta_i); & z > 0 \\ S(\theta_i)\exp(\kappa_i z)\exp(ikx\sin\theta_i); & z < 0 \end{cases}$$

is the unperturbed wave field for the flat wall, with

$$R(\theta_i) = \frac{k\cos\theta_i - i\kappa_i}{k\cos\theta_i + i\kappa_i}$$

and

$$S(\theta_i) = 1 + R(\theta_i); \quad \kappa_i = \sqrt{k_c^2 - k^2\cos^2\theta_i}.$$

$\psi_1^{(1)}(\mathbf{r})$ and $\psi_1^{(2)}(\mathbf{r})$ denote the first- and second-order perturbation terms.

Keeping terms $\sim \eta^1$ in R, S, etc., we obtain the absorption corrections to the specular and scattered beams and, by comparison of net outgoing to incoming intensities, the loss coefficient for the rough wall. For details of the analysis see Appendix C. Here we summarize the main results for the intensities normalized to the incident flux. Taking the squared magnitude of (12) (outgoing waves only) results in cross terms labeled by (mn) where $m, n = 0, 1, 2$ stands for the order of perturbation:

(i) (0,0): Specular reflectivity for the flat wall, derived from $|\psi_0|^2$: $I_{(00)} = |R(\theta_i)|^2 = 1 - \mu_0(\theta_i)$, where $\mu_0(\theta_i) = 2\eta k\cos(\theta_i)/\kappa_{i0}$ is the absorption coefficient for incidence at angle θ_i on a flat wall [7–9], with $\kappa_{i0} = (k_{c0}^2 - k^2\cos^2\theta_i)^{1/2}$.

(ii) (0,1): Interference term with first-order perturbation for specular reflection, arising from $2Re(\psi_{0r}^*\psi_1^{(1)})$:

$$I_{(01)} = -\mu_0(\theta_i)k_{c0}^2 b^2. \tag{13}$$

For $\eta = 0$, there is no first-order interference. This shows that a "Debye-Waller factor" for specular beam attenuation cannot be obtained from first-order perturbation.

(iii) (1,1): The first-order intensity scattered into unit solid angle at (θ, φ) is given by the outgoing flux with density $|\psi_1^{(1)}(\mathbf{r})|^2$, normalized to the incident flux, with the result (for UCN)

$$I_{(11)} = 4k^4\cos\theta_i\cos^2\theta F(q) \times\left[1 - \eta\left(\frac{k\cos\theta_i}{\kappa_{i0}} + \frac{k\cos\theta}{\kappa_0}\right)\right], \tag{14}$$

where

$$F(\mathbf{q}) = F(q) = \frac{1}{(2\pi)^2}\int_A f(\delta)e^{-i\mathbf{q}\cdot\boldsymbol{\delta}}d^2\boldsymbol{\delta} \tag{15}$$

is the Fourier transform of the height-height correlation function (1) and represents the roughness spectrum [4]. For $\eta = 0$, and for UCN (rather than cold neutrons in general), Eq. (14) agrees with Eq. (20) of Ref. [4]. Removing common constants, we write $F(q) = [b^2w^2/(2\pi)]L(q)$, where

$L(q) = \exp(-q^2w^2/2)$ for the Gaussian model, and (16a)

$$L(q) = \frac{2t}{(1 + 2q^2w^2)^{1/2}}\frac{K_1[t(1 + 2q^2w^2)^{1/2}]}{K_0(t)}$$

for the "K_0 model" with $t = 0.7709$. (16b)

From (14) we obtain the total diffusely scattered intensity up to terms $\sim b^2$ and η^1:

$$p_D = p_{D0} - 2k^4\cos\theta_i\int_{(2\pi)}d\Omega\cos^2\theta[\mu_0(\theta_i) + \mu_0(\theta)]F(q), \tag{17}$$

where

$$p_{D0} = 4k^4\cos\theta_i\int_{(2\pi)}d\Omega\cos^2\theta F(q) \tag{18}$$

is the total scattered intensity for $\eta = 0$, and $\mu_0(\theta) = 2\eta k \cos\theta/(k_{c0}^2 - k^2\cos^2\theta)^{1/2}$ is the flat-wall loss coefficient for angle θ. For $\alpha \ll 1$ the scattered intensity $I_{(11)}$ forms a halo around the specular beam with small width of order α, as expected from ray optics.

(iv) (0,2): Interference of specular reflection with second-order perturbation, arising from $2Re(\psi_{0r}^* \psi_1^{(2)})$:

$$I_{(02)} = -p_{D0}[1 - \mu_0(\theta_i)] + k^2 k_{c0}^2 \cos\theta_i \times \int_{(2\pi)} d\Omega \mu_0(\theta) F(q). \quad (19)$$

For $\eta = 0$, this term is required to satisfy unitarity. Up to order b^2, the total outgoing intensity (specular plus diffuse) equals the incoming intensity. In other words, the "Debye-Waller" attenuation factor DWF for the specular beam equals $1 - p_{D0}$, as it should. Carrying out the integration for p_{D0} we find that the DWF is close to but not identical to the factor $\exp(-4b^2k^2\cos^2\theta_i) \sim 1 - 4b^2k^2\cos^2\theta_i$ given in Ref. [5]. At this point it should also be mentioned (as is in Ref. [5]) that to arrive at the common Gaussian form for a DWF one has to make the drastic assumption that the wave inside the medium is given by the same function as the wave outside the medium, throughout the rough layer. This is not plausible for larger roughness, especially not for UCN, since only ψ and its first derivative $\partial\psi/\partial z$ are continuous at the surface. Using (13) and (19) we obtain the Debye-Waller factor for an absorbing, rough wall: DWF $= |R|^2 + I_{(01)} + I_{(02)}$ (up to terms $\sim b^2$ and $\sim \eta$).

(v) Combining the terms (0,0), (0,1), (1,1), and (0,2) we obtain the absorption coefficient for a rough wall:

$$\begin{aligned}\mu(\theta_i) &= (\text{incoming flux} - \text{outgoing flux})/(\text{incoming flux}) \\ &= 1 - (I_{(00)} + I_{(01)} + I_{(02)}) - \int_{(2\pi)} d\Omega I_{(11)} \\ &= \mu_0(\theta_i)\left(1 + k_{c0}^2 b^2\right) - 2k^4 \cos\theta_i \int_{(2\pi)} d\Omega \cos^2\theta \\ &\quad \times [\mu_0(\theta_i) - \mu_0(\theta)] F(q) - k^2 k_{c0}^2 \cos\theta_i \\ &\quad \times \int_{(2\pi)} d\Omega \mu_0(\theta) F(q). \end{aligned} \quad (20)$$

This agrees with the result derived in Ref. [7] using a somewhat different approach. Numerical results were not given in Ref. [7]. Higher-order perturbation would yield only terms $\sim b^n$ with $n > 2$.

V. APPROXIMATIONS AND NUMERICAL RESULTS

Numerical evaluation of the double integrals over θ and φ in (17)–(20) is greatly facilitated if one of the integrations can be performed analytically. For the Gaussian model, the φ integration leads to the Bessel function I_0, but no analytical solution is known for the "K_0-model." Using the transformation $k^2 d\Omega \cos\theta = d^2\mathbf{q} = k^2 \nu d\nu d\psi$, with $q = k\nu$, the ψ integration can be performed analytically for any roughness model since $F(q)$ only depends on ν, not on ψ. It is evident from Fig. 1 that for $\nu < 1 - s_i$ (with $s_i = \sin\theta_i$), the ψ integration runs from $-\pi$ to $+\pi$. For $1 - s_i < \nu < 1 + s_i$, the limits are $\pm\psi_u$ with $\sin^2(\psi_u/2)) = [1 - (\nu - s_i)^2]/(4\nu s_i)$. Expressing $\cos\theta$ in terms of ν and ψ as $\cos^2\theta = 1 - (s_i - \nu)^2 - 4\nu s_i \sin^2(\psi/2)$, the ψ integrations in (17)–(20) can be performed analytically in terms of elliptic integrals, as shown in Appendix D.

Before proceeding with numerical results, we point out the special case of fairly smooth surfaces with small mean-square slope ($\alpha^2 \ll 1$) and a UCN wavelength small on the scale of the lateral correlation length w, viz. $kw \gg 1$. Smooth surfaces are expected to form when a special low-temperature oil, "LTF" [10], is sputtered onto a cold surface and then thermally cycled by slow liquefaction and refreezing, as in Ref. [3]. Under these circumstances, $F(\nu)$ is very small for $\nu \gg (kw)^{-1}$ and the ν integration can be extended to ∞. In this case, model-independent results are obtained as follows: The analytical expressions for the ψ integrals are expanded for small ν as $I_\psi = a_0 + a_2\nu^2 + a_4\nu^4 + \cdots$ and we use the identities

$$2\pi \int_0^\infty q dq F(q) = f(0) = b^2 \quad (21)$$

$$2\pi \int_0^\infty q^3 dq F(q) = g(0) = \alpha^2 \quad (22)$$

$$2\pi \int_0^\infty q^5 dq F(q) = 4h(0) = 4\kappa^2, \quad (23)$$

which follow from the properties of Fourier transform (15) and relations (4) and (7) among $f(\delta)$, $g(\delta)$, and $h(\delta)$.

In this way asymptotic expressions are obtained for p_{D0} and $\Delta\mu(\theta_i)/\mu_0(\theta_i) = [\mu(\theta_i) - \mu_0(\theta_i)]/\mu_0(\theta_i)$:

$$p_{D0}(\theta_i) = 4k^2b^2 \left\{ c_i^2 - \frac{1 + c_i^2}{2c_i^2} \frac{1}{(kw)^2} + O[(kw)^{-4}] \right\} \quad (24)$$

and

$$\Delta\mu(\theta_i)/\mu_0(\theta_i) = -\frac{\alpha^2}{2\left(1 - \zeta^2 c_i^2\right)} \left\{ 1 - \frac{1}{2}\frac{s_i^2}{c_i^2}\frac{2 + \zeta^2 c_i^2}{1 - \zeta^2 c_i^2} + O[(kw)^{-2}] \right\}, \quad (25)$$

where $\zeta = k/k_{c0} \leqslant 1$ and $c_i = \cos\theta_i$. For perturbation theory to be valid, $p_{D0}(\theta_i)$ must be $\ll 1$ over the entire range of θ_i.

Taking only the first term in the curly bracket ($p_{D0} \approx 4b^2k^2\cos^2\theta_i$), Eq. (24) is consistent with the usual DWF with expansion $(1 - 4b^2k^2\cos^2\theta_i + \cdots)$, which is the standard Born approximation result of Ref. [5] (see also Ref. [11]). Note that for $\eta = 0$ the loss of specular intensity, 1-DWF, equals $p_{D0}(\theta_i)$ [6], thus particle number is conserved. Figure 2 compares approximation (24) (first term only) with the exact numerical result for $k_{c0} = 0.0802\ \text{nm}^{-1}$, $\alpha = 10^{-3}$, and $w = 2\ \mu\text{m}$ ($b = \alpha w/\sqrt{2} = 1.4$ nm). The critical value k_{c0} is for the LTF oil in its glass state at ~110 K used in Ref. [3]. The agreement is excellent, indicating that for these parameters the Born approximation for the DWF is adequate. The numerical values of p_{D0} for the Gaussian model are very similar to those of the K_0 model used for Fig. 2.

On a general basis, for $\alpha^2 \ll 1$ the approximations (24)–(25) are valid over a wide range of θ_i but not near grazing incidence ($\theta_i \to \pi/2$) since in this range $(1 - s_i)kw$ is *not* $\gg 1$.

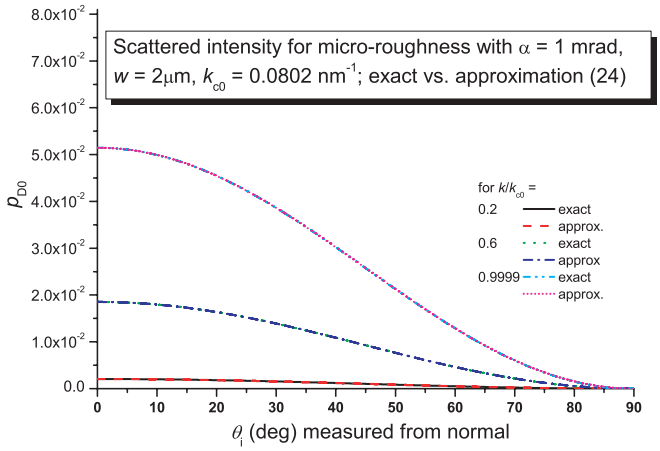

FIG. 2. (Color online) The total diffusely scattered intensity p_{D0} [from (18) for the K_0 model] is compared to approximation (24) which is valid for fairly smooth roughness ($\alpha \ll 1$). For the parameters used the agreement is excellent.

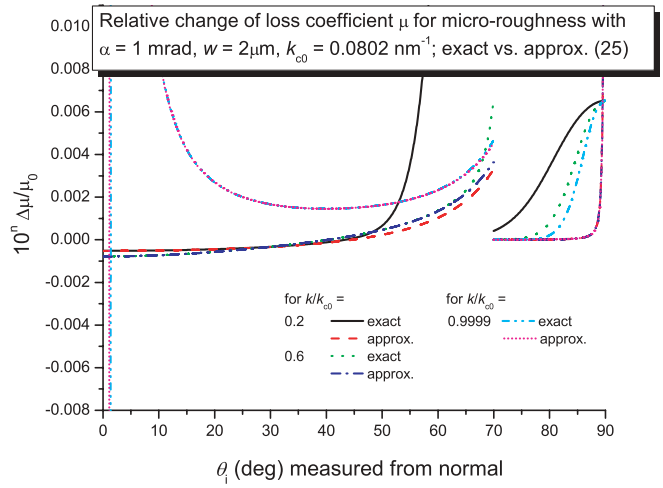

FIG. 3. (Color online) Angle dependence of roughness correction to the wall loss coefficient, $\Delta\mu(\theta_i)/\mu_0(\theta_i)$. The numerical result from (20) for the K_0 model is compared to approximation (25). The agreement is very good except for θ_i near 90° (glancing incidence). In this plot the scale changes from $n = 3$ (expanded scale) for $\theta_i < 70°$ to $n = 1$ (direct scale) for $\theta_i > 70°$.

Therefore the ν range for integration over the full ψ range from $-\pi$ to $+\pi$ (see Fig. 1) cannot be extended to ∞.

From (25) we deduce a perhaps unexpected result: over a significant range of θ_i, namely where the curly bracket is positive (for $\zeta \ll 1$: $\theta_i < 45°$), the loss coefficient for the rough surface, $\mu(\theta_i)$, is somewhat smaller than that for the flat wall, $\mu_0(\theta_i)$, with a relative difference of order α^2. This contradicts a general statement in Ref. [7] (see p. 185), while a decrease was predicted for a certain model in Ref. [12]. The decrease found here for $\alpha \ll 1$ is independent of the model and is plausible for a geometric-optics picture, where geometric reflections for the local surface orientation are incoherently superposed: For near-normal incidence the mean angle for incidence on inclined patches of a rough surface is always larger than for the flat surface, for which it is zero for $\theta_i = 0$, and therefore the factor $[k_{c0}^2 - k^2\cos^2(\theta_i)]^{-1/2}$ in $\mu_0(\theta_i)$ is reduced, on average. No reduction of $\mu_0(\theta_i)$ is seen for "jagged" roughness with α of order 1.

For the same values of α, etc., as for Fig. 2, Fig. 3 shows a comparison of numerical results for $\Delta\mu(\theta_i)/\mu_0(\theta_i)$ with approximation (25) for the K_0 model. Again, the approximation clearly fails for grazing incidence [both (24) and (25) diverge as $\theta_i \to \pi/2$] but is an excellent representation at steeper incidence. The Gauss and K_0 model give very similar results.

For UCN confined in a trap the angular distribution is, in most cases, assumed to be close to isotropic (although deviations are critical, see below). To obtain directional averages of p_{D0} and $\Delta\mu$ the region of grazing incidence that is not described by (24)–(25) has to be included, and it makes a significant contribution. The angular dependence of $\Delta\mu(\theta_i)/\mu_0(\theta_i)$ for the Gauss model (not shown in Figs. 2 and 3) with the same parameters is close to that for the K_0 model and the isotropic mean values

$$\langle Z\rangle = 2\int_0^1 c_i\,dc_i\,Z(\theta_i) \tag{26}$$

agree within 15%. Figure 4 shows the ζ dependence of $\langle\Delta\mu\rangle/\langle\mu_0\rangle$ for both models. The reference average for the flat wall is given as [7–9]

$$\langle\mu_0\rangle = 2\eta[\arcsin\zeta - \zeta(1-\zeta^2)^{1/2}]/\zeta^2 \to \begin{cases} 4\eta\zeta/3 & \text{for} \quad \zeta \ll 1 \\ \pi\eta & \text{for} \quad \zeta = 1. \end{cases} \tag{27}$$

The main features of $\langle\Delta\mu\rangle/\langle\mu_0\rangle$ are a sharp peak of height $(bk_{c0})^2$ at $\zeta = 0$ with half-width $\Delta\zeta \sim \sqrt{2}/(wk_{c0})$ and a drop-off approximately $\sim \zeta^{-3/2}$. A reasonable fit, with maximum deviations of $\sim 20\%$ over a wide range of k_{c0} and of (small) α and b and (large) w, both to the Gauss- and K_0 micro-roughness

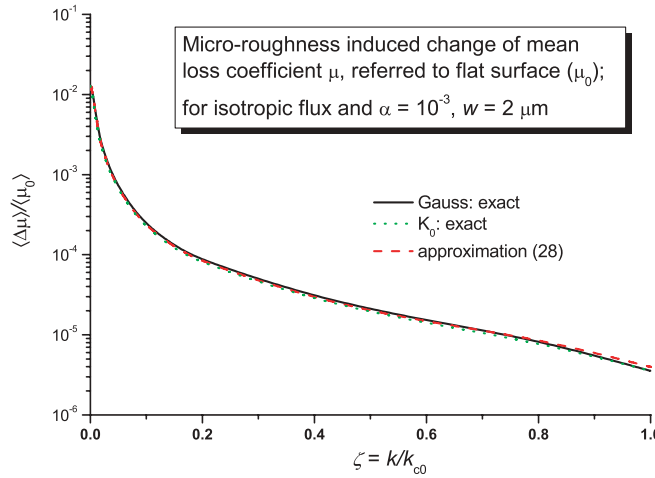

FIG. 4. (Color online) Mean value of roughness correction, $\langle\Delta\mu(\theta_i)\rangle$, for isotropic UCN flux, referred to the flat-wall average $\langle\mu_0(\theta_i)\rangle$ given in (27). For the parameters given, the numerical result for both models are compared to the semianalytical approximation (28). Both for the Gauss and the K_0 model, the agreement is reasonably good, with maximal deviations of ~20% over a wide range of parameters.

models, is

$$\frac{\langle \Delta\mu \rangle}{\langle \mu_0 \rangle} \cong k_{c0}^2 b^2 [1 + 3(\zeta k_{c0} w/2)^2]^{-3/4} \left(1 - \frac{1}{2}\zeta^4\right) \tag{28}$$

which is shown as the dashed curve in Fig. 4. The isotropic-flux average of diffuse fraction p_{D0} is

$$\langle p_{D0} \rangle = 2k^2 b^2 \tag{29}$$

where we used the one-term approximation of (24).

In applications to actual UCN storage, approximations (28) and (29) can be used to determine further averages analytically. For a monochromatic UCN spectrum under gravity the averaging is over wall-interaction height h from the trap bottom to the "roof" or to the maximum height reachable for a given energy (h_0, in units of maximum jump height). Further averaging over the spectrum (over h_0) is usually also required. For instance, the sharp peak of $\langle \Delta\mu(\theta_i) \rangle / \langle \mu_0(\theta_i) \rangle$ at $\zeta = 0$ implies a large loss rate for UCN in contact with the wall near their maximum jump height h_0 where $\zeta \to 0$. Taking into account that the flux [$\sim(h_0 - h)dS$] incident on surface element dS vanishes as $h \to h_0$, a detailed analysis is required. It shows that the loss enhancement strongly depends on the trap geometry and UCN energy and is significant for very low energy UCN "hopping" in small jumps on an essentially flat horizontal surface, for instance the rim of a cylinder with horizontal axis, as in Ref. [3].

VI. DETAILED BALANCE REQUIREMENT AND SIMPLIFICATIONS

A trapped UCN gas will acquire or maintain an equilibrium isotropic distribution only if its interaction with a rough wall (or magnetic field irregularities) satisfies the detailed balance requirement discussed in Ref. [7] (see p. 96). The flux undergoing scattering from solid angle $\Omega_i = (\theta_i, \varphi_i)$ to $\Omega = (\theta, \varphi)$ must equal the flux for the reverse process $\Omega \to \Omega_i$, in accordance with the fundamental principles of time-reversal invariance and micro-reversibility. Since the flux incident at Ω_i (or Ω) is proportional to $\cos\theta_i$ (respectively $\cos\theta$) any diffuse scattering distribution $I_{sc}(\Omega_i \to \Omega)$ must satisfy the symmetry requirement

$$I_{sc}(\Omega_i \to \Omega) = \tilde{I}(\Omega_i, \Omega) \cos\theta, \tag{30}$$

where $\tilde{I}(\Omega_i, \Omega)$ is a function symmetric in (θ_i, θ) and (φ_i, φ) and $\cos\theta$ is the Lambert factor. The scattering distribution $I_{(11)}$ of Eq. (14) satisfies this requirement.

Various simplifications of the micro-roughness scattering distribution (14) (for $\eta = 0$) have been used in Refs. [13–15]. The limit of maximal diffusivity is reached for a "dense roughness" model where $kw \to 0$, hence $\alpha \sim b/w \to \infty$. This leads to [14,15]

$$I_{\rm sc} \cong B\,[\cos\theta_i \cos\theta] \cos\theta \tag{31}$$

with $B = 2k^4 b^2 w^2/\pi$ and a diffuse fraction $p_{D0} = (2\pi/3) B \cos\theta_i$ that depends on incident angle θ_i and UCN energy ($\sim k^2$). It has been pointed out in Ref. [15] that for kb at most of order 1, as required for perturbation theory to be valid [4], the limit $kw \to 0$, hence $B \to 0$, is strictly justifiable only for very small diffuse fraction p_{D0}.

As a further simplification, averaging over incident energy may be performed but could be a coarse approximation for broad spectra, as for confined UCN. To arrive at the simplest form of (30), with $\tilde{I} = \text{const.}$, requires further averaging of $[\cos\theta_i \cos\theta]$ in (31). Assuming isotropic distributions in θ_i and θ we obtain $\langle \cos\theta_i \cos\theta \rangle = 4/9$. Thus, (31) becomes

$$\langle I_{\rm sc} \rangle = \langle \tilde{I} \rangle \cos\theta \tag{32}$$

with $\langle \tilde{I} \rangle = 8\langle k^4 \rangle b^2 w^2/(9\pi)$ and a total diffuse fraction $\langle p_{D0} \rangle = \pi \langle \tilde{I} \rangle$. Like (31), Eq. (32) is justified only for small $\langle p_{D0} \rangle$.

In the "dense roughness" limit the loss coefficient $\mu(\theta_i)$ of (20) can be averaged analytically [7] with the result $\langle \mu \rangle \cong \langle \mu_0 \rangle (1 + k_{c0}^2 b^2)$, where $\langle \mu_0 \rangle$ is given in (27). However, except for very small $\langle p_{D0} \rangle$ the correction term $k_{c0}^2 b^2 \cong k_{c0}^4 \langle p_{D0} \rangle / (\langle k^4 \rangle w^2)$ would become large as $k_{c0} w \to 0$, conflicting with the perturbation theory requirement.

It should also be noted that in averaging over θ_i we lose the proportionality of $I_{\rm sc}$ to $\cos\theta_i$ which implies a small scattering probability for glancing incidence ($\theta_i \to \pi/2$). For UCN stored in traps with high geometrical symmetry this dependence can give rise to almost stationary orbits for UCN "sliding" along a concave surface (see Sec. VIII). For other geometries, only a few reflections, or where these details are not important, as in the computer code tests of Ref. [13], (32) is a useful, simple approximation satisfying detailed balance.

As an example of a roughness model that does not satisfy detailed balance we mention the scattering distribution (E6) derived in Appendix E for the macroscopic, ray optics limit. In this case, $I_{\rm sc}$ is symmetrical in (θ_i, θ) and (φ_i, φ), lacking the extra factor $\cos\theta$. This violation of detailed balance can be tolerated if only a few reflections have to be considered, as in a neutron guide [4], but attempting to use this model for thousands of consecutive reflections in a Monte Carlo simulation, as required for long UCN storage (see below), results in the loss of isotropic equilibrium. We observed that UCN accumulated in grazing-angle orbits, depleting other regions of phase space.

VII. MONTE CARLO SIMULATION TECHNIQUES

In Monte Carlo simulations of UCN propagation and storage, as in Refs. [7,14,15], two complementary ways of implementing a given scattering probability distribution $P(\theta, \varphi)$, e.g., Eq. (14), have been discussed and used.

The inversion method (for UCN see Ref. [7], p. 98) is based on mapping the joint probability distribution $P(\theta, \varphi)$ onto the ranges 0 to 1 of uniformly distributed random numbers (r.n.) x, y, z, and so on. For instance, for the "dense roughness" limit $I_{\rm sc} = (\text{const.}) \cos^n\theta$, with $n = 2$ for Eq. (31) and $n = 1$ for (32), we can set $\varphi/(2\pi) = x - \frac{1}{2}$ and $\cos\theta = y^{\frac{1}{(n+1)}}$.

For more complex scattering functions like (18) we chose von Neumann's acceptance or rejection method that was first applied to UCN in Ref. [15]. In general, it involves "rolling the dice" repeatedly until a combination of x, y, z satisfying $P(\theta, \varphi)$ is found. Specifically for UCN, this method can be greatly abbreviated if $P_{\max}$, the maximum value of $P(\theta, \varphi)$

for given θ_i and k, satisfies $2\pi P_{\max} < 1$. In this case, the reflection is considered specular if $z > 2\pi P(\theta, \varphi)$. Otherwise, it is diffuse with angles determined as $\varphi/(2\pi) = x - \frac{1}{2}$ and $\cos\theta = y$.

In all these schemes, wall losses and β decay are irrelevant for the choice of reflection angles. However, we keep track of the accumulation of net loss at each reflection and use the overall loss factor as a weighting factor for UCN that have survived losses and can be counted in a detector. The loss factor contained the second-order correction of Eq. (20) and was implemented in tabulated form.

VIII. MONTE CARLO SIMULATION FOR NEUTRON LIFETIME EXPERIMENT [3]

The neutron lifetime experiment [3] reports a value $\tau_n = 878.5 \pm 0.7_{\text{stat}} \pm 0.3_{\text{sys}}$ s which is 7.2 s (or 0.8%, or >6 standard deviations) away from the current particle data world average 885.7 ± 0.8 s [2]. The quoted precision is better than for any previous single lifetime measurement. Since data interpretation for this experiment relied heavily on computer simulations we have performed independent simulations using the roughness model outlined above. In this system [3,16], shown in Fig. 5, a cylindrical or a "quasispherical" vessel with an opening rotates about a horizontal axis during the various steps of a cycle: Filling with UCN with the hole pointing straight down; rotation to a "monitoring position" for spectral cleaning; storage for a "short" time (300 s) or a "long time" (2000 s) with the hole in the upright position; then emptying in five steps at intermediary angles. This scheme provides for a spectral analysis, with a batch of higher-energy UCN counted first and the slowest UCN pouring out at the last stage

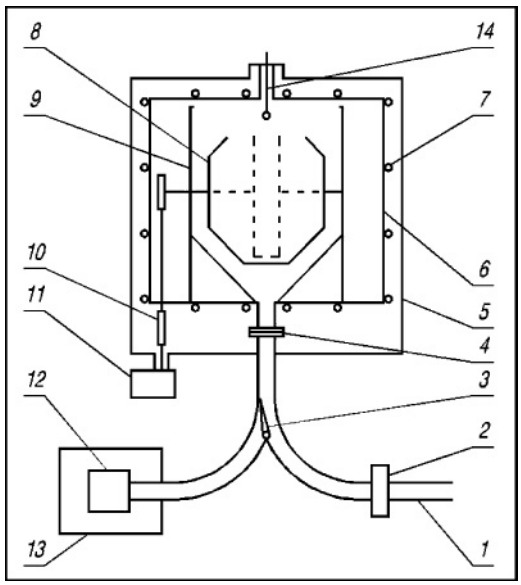

FIG. 5. Schematic of the apparatus used in Ref. [3]. UCN from a guide tube 1 pass through a large entrance or exit channel to a cylindrical or "quasispherical" storage chamber 8 that can be rotated about a horizontal axis. After a short or long holding time, UCN in five spectral ranges are, successively, discharged through the same channel to the detector 12. The system 14 is used to coat the walls with a special low-temperature oil.

while the opening moves to the vertical down position. The detailed measuring scheme [3] is complex, involving not only energy-dependent data for the five energy bins but also traps with different mean free path for the UCN. This combination allows, both "energy extrapolation" and "size extrapolation" to the neutron lifetime.

Data analysis is also complex, relying heavily on computer simulation to determine the parameter $\langle\gamma\rangle = \langle\mu f\rangle/\eta$ against which measured inverse storage lifetimes are plotted for the extrapolation. The average $\langle\mu f\rangle$, with wall collision frequency f, is the wall loss rate (mean loss per second).

For a narrow cylindrical trap the authors of Ref. [3] compared simulations with the measured time spectra for the first counting interval following short storage (300 s) (see Fig. 14, lower part, in Ref. [3]). They concluded that a certain minimum roughness (diffuse fraction $\geqslant 1\%$) of the trap wall was required to obtain agreement. This is a crucial step with respect to the neutron lifetime, and therefore we have performed independent simulations of short and long storage cycles for a narrow cylindrical vessel with radius 38 cm, width 14 cm, and aperture 62° for the opening, to investigate this issue using the near-mirror reflection model with long-range roughness ($\alpha \ll 1$) described above.

In our simulation UCN are generated at the beginning of the monitoring phase (at trap angle 30°) over a horizontal sheet in the lower half of the trap: at a height $z_0 = (2/3)h_0$ for $h_0 \leqslant (3/2)R$ and at $z_0 = R$ for $h_0 > (3/2)R$. Even for highly specular reflection on the oblique channel walls, including the cone and the trap exterior, the UCN in the wide channel section around the trap will have reached a highly isotropic distribution within the 160 s of channel loading. Thus the UCN entering the trap, mainly during rotation from 180° to 30° at the end of loading, are essentially isotropic and their initial flight angle θ, referred to the up and down directions, may be derived from a r.n. x as $\cos\theta = x^{1/2}$. The energy distribution is the same as used in Ref. [3], namely the Maxwell distribution modified by a heuristic attenuation factor $\exp(-h_0/h_{\text{sp}})$ with $h_{\text{sp}} = 0.6$ m (not specified in Ref. [3]). We used a maximum (minimum) energy of 0.95 m (0.05 m).

The time sequence of monitoring, storage, and emptying in five steps was the same as described in Ref. [3]. The wall reflections were assumed elastic except for the (very small) Doppler shift for wall reflections during times when the trap rotates at 5.1°/s (respectively 17°/s on the way from 0° to 40° for a rotation time of 2.3 s [3]) and the reflection is diffuse. For perfectly cylindrical geometry the overall shift is very small. Reflection points were calculated analytically from the previous reflection position, energy, and take-off angle, assuming perfectly cylindrical geometry. At each reflection, the wall loss was incremented according to the loss coefficient μ for this reflection. A run was terminated at the time when the UCN passed through the opening without immediately falling back into the trap. For the purpose of this work the exit channel could be neglected and those UCN that had escaped loss, as determined by the integrated loss including β decay, were counted into time bins of 10-s or 1-s resolution. For consistency with [3] we used the quoted values $\eta = 2 \times 10^{-6}$ and $\tau_n = 878.5$ s in the simulation. The bins were combined to the five counting intervals, and short runs with storage time

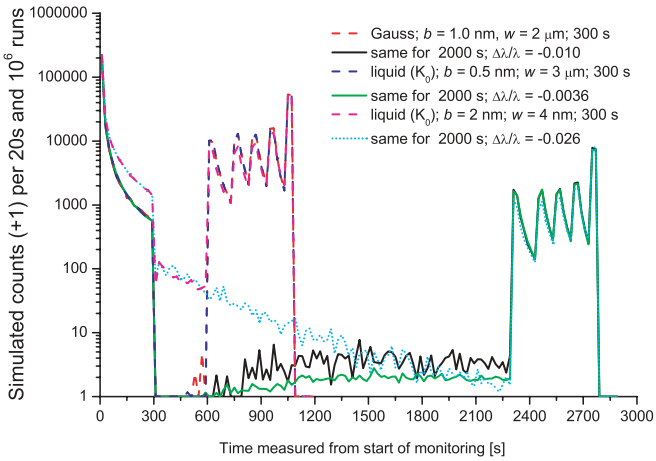

FIG. 6. (Color online) Simulated count rates, in 20-s bins, versus cycle time t, starting from "monitoring" for 300 s where the trap is at hold position 30° titled away from vertical. The data are normalized to 10^6 runs (one run for each UCN started at $t = 0$). Data are shown for both short and long storage and for both the Gauss and K_0 models for a fairly smooth surface with similar parameters, as shown in the inset. They correspond to $\alpha = 7.1 \times 10^{-4}$ for the Gauss model, and $\alpha = 2.4 \times 10^{-4}$ for K_0. An example of steeper roughness ($\alpha = 0.7$) is shown for comparison. We plot the simulated counts N *plus one* to allow a distinction between $N = 0$ and $N = 1$ on the log scale. In the simulations of Fig. 6 (only) we used a constant angular speed of 4.3°/s for all trap rotations.

300 s were compared to long runs (2000 s) as in the actual experiment to obtain the storage lifetime as a function of mean values $\langle\gamma\rangle$ that were also calculated for each counting interval.

Figure 6 shows simulated count rates, in 20-s bins, versus cycle time t, starting from "monitoring" for 300 s where the trap is at position 30° tilted away from vertical. The data are normalized to 10^6 runs (one run for each UCN started at $t = 0$). Data are shown for both short and long storage and for both the Gauss and K_0 models, for a fairly smooth surface with similar parameters, as shown in the inset. They correspond to $\alpha = 7.1 \times 10^{-4}$ for the Gauss model and $\alpha = 2.4 \times 10^{-4}$ for K_0. An example of steeper roughness with $\alpha = 0.7$ (for $b = 2$ nm and $w = 4$ nm) is shown for comparison.

We will focus on three features of Fig. 6 and their implications: First, on the time spectra for the first counting interval following short storage ($t = 600-750$ s); second, on the spectra following, and including, trap rotation to vertically up for holding ($t = 300-600$ s); and third, the count rates during long storage ($t = 300-2000$ s).

A. First counting peak

To allow a comparison with the time spectra for the first peak measured in Ref. [3], we show in Fig. 7, at a higher resolution of 1 to 2 s, an expanded view of the interval from 600 to 750 s (on the time scale of Fig. 14 in Ref. [3] this corresponds to the interval 760 to 910 s). The data of Ref. [3] are included in Fig. 7 as curves 1 and 2. Prior to discussion we point out differences between the two simulation approaches.

The authors of Ref. [3] used a roughness model characterized by a single number, the diffuse fraction for the trap

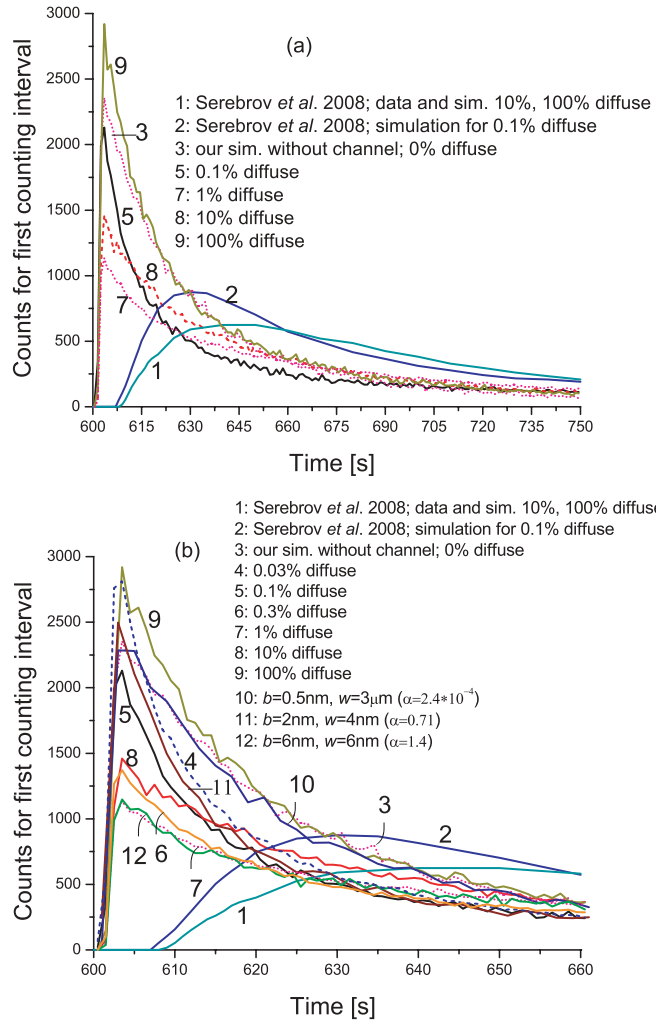

FIG. 7. (Color online) Comparison of measured (Serebrov *et al.*, 2008: [3]) and simulated time spectra for the first counting period following short storage. For clarity, (b) shows an expanded view of the initial 60 s of the full 150-s interval shown in (a). Some of the simulation curves of (b) are also included in (a). For a discussion see the text.

walls, but did not state which roughness model was used. The simulation included the exit channel (designated secondary volume and UCN guide in Ref. [3]) but the authors did not describe the geometrical model used for this complex structure. It included (see Fig. 5) the trap exterior and interior (which some UCN temporarily re-enter on their way to the detector), the wide conical channel section, the valve selector with its gaps, the curved guide, and the detector with its window that accumulated an oil film as a result of repeated surface coating using the evaporator 14 shown in Fig. 5. The surface properties, including roughness, of the oil-coated channel walls with their temperature gradient, varying from the trap temperature to near-room temperature for the detector, are not discussed.

Our simulation did not include the exit channel. We used the roughness models and parameters listed for curves 3–12 of Fig. 7. In Fig. 7(b) the initial part is expanded for clarity. For these counting spectra following short storage the details of wall loss are insignificant and the results using

(20) are indistinguishable from those for the elementary, flat-wall expression that was used in Ref. [3]. (During the long holding period of 2000 s the details of loss coefficient may become important, depending on the roughness parameters.)

Curve 1 represents the measured data (Fig. 14 of Ref. [3]), using a scale approximately adjusted to counts per 2 s for 10^6 initial UCN. Curve 1 practically coincides with the Ref. [3] simulations for 10% and 100% diffusivity. Curve 2 is the simulation, in Ref. [3], for 0.1% diffusivity. Curve 3 is our simulation (for the trap only) for an ideally smooth surface. For curves 4–9 we used the simplest scattering distribution consistent with detailed balance, Eq. (32), with diffuse fractions 0.03, 0.1, 0.3, 1, 10, and 100%. For consistency with Ref. [3], we included large values of $\langle p_{D0}\rangle$, disregarding the restriction outlined following Eq. (31). Curves 10–12 are based on the micro-roughness result (14) (for $\eta = 0$) and the K_0 model. The parameters for curves 10–12 represent increasingly steeper roughness ($\alpha = 2.4 \times 10^{-4}$, 0.71, and 1.4) and increasing $\langle p_{D0}\rangle$ (0.16, 0.55, and 11.3%, where the last value is at the limit of perturbation theory validity).

Figure 7 shows the large spectral distortion and time delay due to the exit channel. The peak widths at half maximum for curves 1 and 2 are 3 to 6 times larger than for the simulations excluding the exit channel. Thus the channel response function to the relatively short pulse of UCN pouring out of the trap essentially determined the measured time spectra.

For consistency with Ref. [3] we focus first on the simulations based on (32). The minimum half-width $\Delta t = 10$ s is observed for $\langle p_{D0}\rangle = 0.1\%$. Both for $\langle p_{D0}\rangle \geqslant 1\%$ and $\langle p_{D0}\rangle \ll 0.1\%$ (including zero), the curves are ~2 times wider, while the curves for 0.03 and 0.3% are intermediary. The difference between 0.1 and $\geqslant 1\%$ diffusivity makes plausible the (much smaller) difference of broadened peaks between the Ref. [3] simulations (including the channel) for $\langle p_{D0}\rangle = 0.1\%$ (curve 2) and 10 or 100% (curve 1). Comparing to the measurement the authors rejected the possibility of diffusivity $\ll 1\%$ for the trap. However, curve 3, for $\langle p_{D0}\rangle = 0$, has about the same larger width, namely $\Delta t = 23$ s, as for $\langle p_{D0}\rangle \geqslant 1\%$ (curves 7–9). The same type of broad line is seen for curve 10 that is based on Eq. (18) for small α. The intermediate (steep) roughness model used for curve 11 (12) results in intermediary (broad-type) linewidths.

The difficulty of distinguishing between roughness models for the trap on the basis of measured curves broadened 3 to 6 times by the response, or resolution, function is exacerbated by two aspects: first, by the uncertainty introduced by any simplification of the complex channel geometry, as needed to make the simulations feasible and, second, in this experiment (and perhaps any UCN experiment conducted so far) neither the primary source intensity and spectrum nor the transmission characteristics of connecting guide tubes, shutters, and other components, here including the channel that is passed by the UCN also during trap loading, is known well in absolute terms. Thus, the area under the counting peak can practically not be used as a criterion for adoption or rejection of a roughness model for the trap. In the present case, the observed variation of peak area in Fig. 7 is a reflection of spectral mixing between the five spectral intervals, as discussed below.

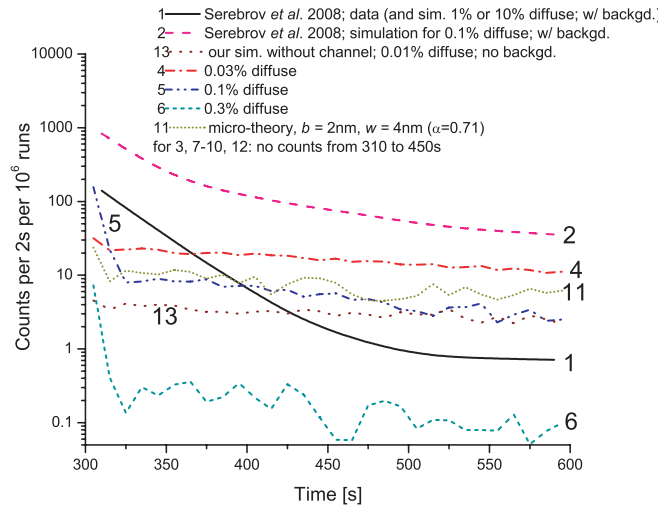

FIG. 8. (Color online) Experimental (Serebrov *et al.*, 2008: [3]) and simulated data are compared for the first 300 s of storage, i.e., from $t = 300$ s to $t = 600$ s. The curves are labeled in the inset. The initial decay, with channel time constant 30 s, for the experimental points (curve 1) and for the simulation in Ref. [3] for isotropic diffusivity 0.1% of surface reflection (curve 2), is due to the last stage of UCN drainage from the wide "entrance or exit channel." The faster initial decrease seen in our simulation data for the trap only (the remaining curves in Fig. 8), occurs because the storage time interval includes the initial 7 s of trap rotation from 30° to 0° [3].

We conclude from this peak analysis that a "soft-roughness" model with $\alpha \ll 1$, as is expected for the temperature-cycled [3] oil-glass coating used, can, probably, not be excluded. Next we discus the second line of reasoning used in [3] to exclude the possibility of surfaces with small isotropic scattering probability (0.1%).

B. Initial count rate during holding

For a narrow trap, Fig. 17 of Ref. [3] shows measured and simulated count rates in the 540s interval following trap rotation from the "monitoring" position at angle 30° to "holding" at 0°. The time of trap rotation from $t = 300$ to $t = 335s$ is included. The simulation contains an unspecified model of the channel, and the background is added. In Fig. 8 we compare these data to our simulations which excluded the channel and the background. As for Fig. 7, the data of Ref. [3] were approximately scaled to simulated counts per 2 s per 10^6 initial UCN, and we used a time scale starting at 300 s, which corresponds to 460 s in Ref. [3].

The measured data (curve 1 in Fig. 8) show the exponential emptying characteristics for the channel, with time constant ~30 s. They essentially agree with the authors' simulations for diffuse fractions 1 and 10% [3]. Curve 2 shows the simulation in Ref. [3] for fraction 0.1% of isotropic diffuse roughness scattering. The remaining curves show our simulations, labeled in the same way as in Fig. 7. We note the following features.

(i) The initial decay with time constant 30 s does not appear in our simulations since it is due to UCN left over in the channel after the preceding monitoring (and channel emptying) phase.

(ii) The simulations for 0.1% (curves 2 and 5) are roughly a factor 10 apart at times $t \geqslant 500$ s, i.e., after complete drainage of the initial channel population. If the scale in Fig. 17 of Ref. [3] is correct, the significant difference underlines the all-important role of the channel and its representation in simulations but will not affect the following conclusions.

(iii) In either case, taking either curve 2 or 5 in Fig. 8 we agree that the case of 0.1% isotropic scattering can be excluded since both curves significantly exceed the measured data (curve 1) in the range $t > 450$ s.

(iv) In the same way, we can exclude curves 13 (0.01%, isotropic), 4 (0.03%, isotropic), and 11 (micro-roughness theory for large-angle roughness with $b = 2$ nm, $w = 4$ nm, hence $\alpha = 0.71$).

(v) As stated in Ref. [3], isotropic fractions $\geqslant$1% (for curves 7, 8, 9, 12, respectively, for 1, 10, and 100% isotropic and $b = w = 6$ nm) are compatible with the measurement, even curve 6 for 0.3% satisfies this criterion.

(vi) However, purely specular reflection (0%, for curve 3 in Fig. 7) as well as long-range roughness with $\alpha \ll 1$, as for 10 ($\alpha = 2.4 \times 10^{-4}$, liquid model) or for $b = 1$ nm, $w = 2$ μm ($\alpha = 7.1 \times 10^{-4}$, Gauss model) are not excluded by the measurement. These models give essentially zero counts in the range $300 < t < 450$ s as shown in Fig. 6 for the latter two cases. The count rate is identically zero during the entire holding period for purely specular, as expected. We have already pointed out that the "soft-roughness" model with $\alpha \ll 1$ is a plausible assumption for the oil-glass coating that reached a mean thickness of order 10 μm after multiple oil evaporations, each of which distributed several cm^3 of oil over the trap plus channel surfaces. While the "soft-roughness" models produce no early counts during the storage intervals (and therefore cannot be rejected), they may give rise to late "spill-over" during the latter part of long storage, as discussed in the next subsection.

C. "Spill-over" during long storage

Returning to Fig. 6, we draw special attention to the finite count rate that appears during the storage intervals, $t = 300$ to 600 s for short storage and $t = 300$ to 2300 s for long storage. At the end of monitoring at trap angle 30° most UCN with energies exceeding the height barrier (~56.5 cm above trap bottom) have spilled out. However, some higher energy UCN move, preferentially, along the cylinder axis and little in other directions. In this highly symmetric trap geometry they have survived in nearly stationary orbits since, for $\alpha \ll 1$, the reflections are nearly mirrorlike with small reorientations of order α if the reflection is diffuse. Thus the random walk toward isotropy is very slow. As the trap rotates to angle 0° at $t = 300$ s the barrier rises by ~14 cm to 70.5 cm from the bottom, and the count rate in Fig. 6 drops to zero. However, since UCN with energies exceeding this new barrier still remain, the same slow relaxation toward isotropy gradually results in steeper orbits. At $t \sim 600$ s some UCN have reached the new barrier and we see a fairly constant "background" count rate throughout the remainder of the long storage interval up to $t = 2300$ s. The range of parameters α, b, and w showing this general tendency is fairly broad, and there is no qualitative difference between Gauss and K_0 models. We will show that this "background" could be overlooked in actual measurements. The same slow diffusion in phase space is also expected to mix the spectral regions for the five counting intervals, and the net result of slow relaxation could give rise to a significant systematic error.

For comparison with experiment [3] we note that the counts in Fig. 6, for 10^6 runs, correspond to ~12 double cycles (one cycle each for short and long storage). The instrument background of ~0.02 s^{-1} (Fig. 10 of Ref. [3]) is equivalent to ~5 counts/20 s in the region 600 s $< t <$ 2300 s of extra holding time for long storage in Fig. 6. This interval has no counts without the relaxation process since the instrument background was not included in our simulations. Thus, the UCN "spilling over the threshold" during this time (~0.8/20 s or 67 in total for the K_0 model) are missing from the UCN count, N_{long}, following long storage, but are not missing from the short-storage counts N_{short}. In the actual experiment the relative change of measured "background" (0.8/5 ~ 15%) is below the significant background variations shown in Fig. 10 of Ref. [3] and would hardly be noticed. However, calculating from $N_{\text{short}}/N_{\text{long}}$ an inverse storage lifetime, $\lambda = 1/\tau_{\text{st}} = [\ln(N_{\text{short}}/N_{\text{long}})]/\Delta t$, with $\Delta t = t_{\text{long}} - t_{\text{short}} = 2300 - 600 = 1700$ s, disregards the "spill-over" and would result in a significant uncertainty of λ, as shown in the following estimation.

We assume that the spill-over rate $n_{\text{spill}}(t)$ originates exclusively from the highest-energy interval #1 (of the 5 intervals) and that entry into (exit from) spectral interval #1 by angular diffusion from (into) #2, or any other interval, is negligible. Thus the number $N_1(t)$ of UCN in #1 decreases during long storage as

$$\frac{1}{N_1(t)}\frac{dN_1}{dt} = -\frac{1}{\tau_{\text{st}}} - \frac{1}{N_1(t)} n_{\text{spill}}(t). \tag{33}$$

In Ref. [3] τ_{st} is close to the lifetime τ_n, so we can approximate $N_1(t)$ by $N_1(t_{\text{short}})\exp[-(t - t_{\text{short}})/\tau_n)]$ in the last term of (33). Integrating (33) from t_{short} to t_{long} and equating $N_1(t_{\text{short}})$ with the counts for interval #1, $N_{1,\text{short}}$, and $N_1(t_{\text{long}})$ with $N_{1,\text{long}}$, we obtain

$$\lambda = \frac{1}{\tau_{\text{st}}} \cong \frac{1}{\Delta t}\ln\frac{N_{1,\text{short}}}{N_{1,\text{long}}} - \frac{C_{\text{spill}}}{N_{1,\text{short}}\Delta t}. \tag{34}$$

The first term on the right is the λ value disregarding spill-over. The second term is the correction with

$$C_{\text{spill}} = \sum_i n_{\text{spill}}(t_i)\exp[(t_i - t_{\text{short}})/\tau_n], \tag{35}$$

where the sum is over the count rates $n_{\text{spill}}(t_i)$ from t_{short} to t_{long}, with a weight factor $\exp[(t_i - t_{\text{short}})/\tau_n]$. Finally, the correction becomes

$$\frac{\Delta\lambda}{\lambda} = -\frac{\Delta\tau_{\text{st}}}{\tau_{\text{st}}} \cong -\frac{\tau_n C_{\text{spill}}}{N_{1,\text{short}}\Delta t}. \tag{36}$$

This value is given in the inset of Fig. 6 and amounts to significant corrections to the inverse storage lifetime for interval #1. If interinterval diffusion is included the values for other spectral intervals, and presumably the energy extrapolation as well, are affected to a significant extent. On the other hand, the measuring scheme of Ref. [3] is more complex, involving also the larger traps including a "quasispherical" vessel, which in the simulations was replaced by a cylinder in a way not discussed in Ref. [3]. We will point out below that our simulation for a fairly smooth surface of a narrow cylindrical trap leads to questions also regarding the x values of the extrapolation, namely the mean values $\langle\gamma\rangle$ for the spectral intervals 1–5.

D. Mean γ values

For the narrow cylindrical vessel, Fig. 9 combines $\langle\gamma\rangle$ values for the five spectral intervals: on the x axis for an "intermediate" roughness with $b = 2$ nm and $w = 4$ nm, and on the y axis for a "smooth" roughness with $b = 0.5$ nm and $w = 3$ μm. The data for short and long storage are plotted separately and the differences are seen to be substantial. They are not explained by the small spectral cooling during storage due to larger wall losses for higher UCN energies. Spectral mixing and spill-over are more important. The large differences are also seen in the mean collision frequencies (not shown) for the five intervals.

E. Mean spectral energies

Spectral mixing is also seen in the "erratic behavior" of mean spectral energies (height $\langle h\rangle$ and difference, $\Delta\langle h\rangle$, between short and long storage). In Fig. 10, $\Delta\langle h\rangle/\langle\langle h\rangle\rangle$ is plotted versus $\langle\langle\gamma\rangle\rangle$ (averaged over long and short storage) for the "smooth" roughness parameters. A spectral change between short and long storage implies a change of detection efficiency that is not discussed in Ref. [3]. While the difference in mean UCN velocity is reduced by the energy boost through the fall height of ~1.5 m between storage vessel and detector, the transparency of the oil-coated detector window for an isotropic UCN beam is a steep function of velocity in the region of interest, with roughly a change of 4 for 1% of UCN energy change. As a result the UCN spend more time in the entrance or exit channel and have a greater chance of being lost, for instance, through gaps.

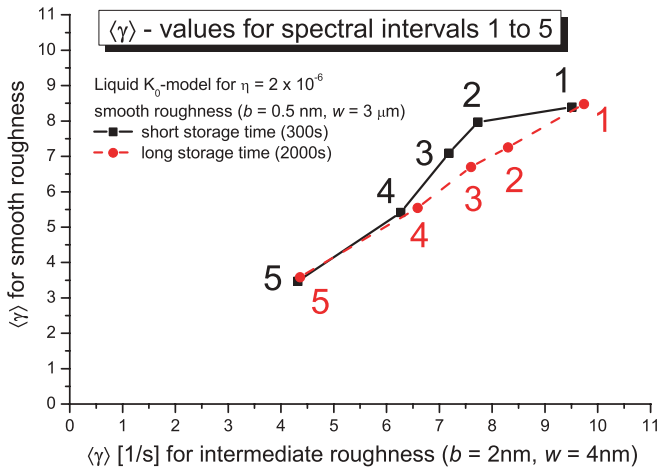

FIG. 9. (Color online) Simulation results for the mean value $\langle\gamma\rangle = \langle\mu\rangle/\eta$, for the five spectral ranges 1 to 5 of Ref. [3], plotted for short storage (300 s, solid lines) and for long storage (2000 s, dashed lines). For the K_0 model, the abscissa shows an example of "intermediary roughness" with $b = 2$ nm, $w = 4$ nm, thus $\alpha = 0.7$. The ordinate values are for $b = 0.5$ nm, $w = 3$ nm, thus $\alpha = 2.4 \times 10^{-4}$. The seemingly "erratic" behavior in either case may be explained by mixing between the five spectral intervals and loss due to "spill-over' during the storage time as discussed in Sec. VIII. The statistical errors for the $\langle\gamma\rangle$ values are insignificantly small.

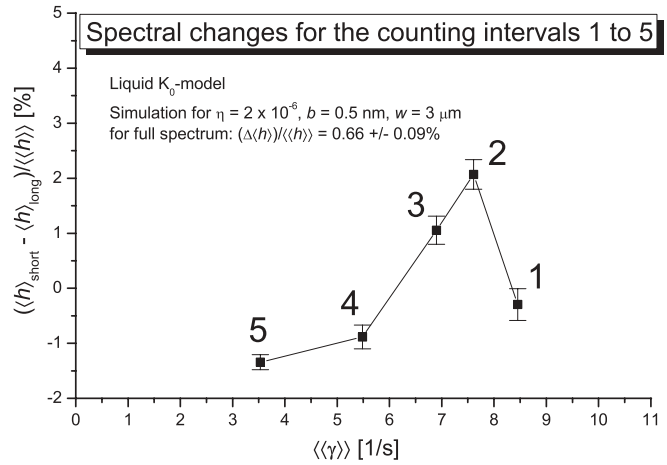

FIG. 10. The "cooling" effect during long storage versus short storage. Instead of a small systematic drop $\langle\Delta h\rangle$ of mean spectral height $\langle h\rangle$ as a function of time, expected since the wall loss increases with UCN energy, the simulation shows fairly large and "erratic" values of $\langle\Delta h\rangle$ for the five spectral ranges. Although there is cooling for the full spectrum, the lowest-energy intervals show negative values of $\langle\Delta h\rangle$ ("heating"). The simulation data are for the K_0 model with fairly "soft roughness" ($\alpha = 2.4 \times 10^{-4}$) and are explained by interspectral mixing and by "spill-over" (see Sec. VIII). The $\langle\langle\gamma\rangle\rangle$ and $\langle\langle h\rangle\rangle$ values are averages over the spectral ranges and over the two storage times (300 s and 2000 s).

F. Extrapolation to the neutron lifetime and the possibility of quasistationary orbits

Figure 16 of Ref. [3] shows an extrapolation plot τ_{st}^{-1} vs. γ for simulations assuming 0.1% isotropic diffusivity. The linear extrapolation would fail due to the "erratic" behavior of τ_{st} as calculated from the five counting peaks for short and long storage. This is of no concern since the case of 0.1% isotropic diffusivity was rejected, both in Ref. [3] and in the present article, as being in conflict with the experimental data.

However, we have shown that the possibility of "soft roughness" ($\alpha \ll 1$) is not excluded by the data. Plots of τ_{st}^{-1} vs. γ for various combinations of b and w, with α of order 10^{-3}, show the same type of irregularity. For instance, for $b = 2$ nm, $w = 2$ μm, ($\alpha = 1.4 \times 10^{-3}$), or for the case of purely specular reflection (shown in Ref. [21]), the mean γ -values for counting intervals 1–3 are not even in sequential order and the values of τ_{st}^{-1} are scattered as in Fig 16 of [3]. A

meaningful linear extrapolation is impossible, irrespective of the short extrapolation distance in γ and τ_{st}.

"Soft roughness," in contrast with dense roughness, gives rise only to small angular changes in diffuse reflections and results in slow diffusion in flight direction away from the orbits for purely specular reflection (with a deviation $\sim N^{1/2}$, where N is the number of diffuse reflections). If quasistationary orbits exist for ideal geometry and surfaces, they also exist in the presence of soft roughness and minor macroscopic deviations from the ideal geometry.

IX. CONCLUSIONS

Using models of microscopic roughness characterized by height-height correlation functions of the Gauss and K_0 type (for solid vs. liquid surfaces), we have carried perturbation calculations to second order, recovering a previous result [7] for roughness-induced wall loss for UCN that has, apparently, found no attention so far. It may be surprising that under certain conditions roughness reduces the wall loss probability. Furthermore, the second-order approach provides absorption corrections to the diffuse scattering distribution as well as the leading terms of a "Debye-Waller factor for roughness" that is consistent with previous derivations but does not require the additional assumption of a height probability distribution function made, e.g., in Refs. [1] and [5]. It is shown that for a fairly smooth wall with small mean-square slope the results are model independent and are determined only by the mean values, mainly for height (b^2) and slope (α^2).

As the central application of roughness scattering we describe independent simulations relating to neutron lifetime experiment [3] which reported a significant deviation from the world average and very high precision. The possibility of a fairly smooth surface for the temperature cycled oil used as the wall coating in this experiment, in connection with the possibility of nearly stationary orbits in any highly symmetric trap geometry, raises questions about the reliability of the extrapolation method used to extract the lifetime value from the storage data.

Note added in revision. A recent comment [22] on the ideas presented here contains explanations relating to two of our questions that had not previously been discussed in Ref. [3]: (a) concerning the roughness model used in Ref. [3] for the trap (and, possibly, channel) surfaces and (b) first information on how the actual roughness of the oil-glass coated surfaces was evaluated.

(i) Two roughness scattering distributions were compared: One is angle independent and violates detailed balance (see our Sec. VI). The second method is described as consistent with Lambert's law. If the underlying model is as detailed for loss calculation in the next-to-last paragraph of Sec. 4 in Ref. [22], it constitutes the ray-optics limit elaborated on in our Sec. VI and Appendix E. Although it also violates detailed balance and results in a loss function inconsistent with the micro-roughness analysis, the ray-optics limit may be considered a passable approximation as long as the mean surface slope $\alpha \ll 1$ and not too many successive reflections are considered. However, for large α the model fails since surface patches of given orientation are too small to be approximated as infinite reflecting planes. No value of α was given in Ref. [22] but α has to be large to comply with the dense roughness requirement for isotropic scattering. Regarding the loss functions $\mu(k) \sim (k/k_{c0})^n$ adopted in Ref. [3] for the surfaces considered as planes, powers $n = 0$, 2, or 3 appear to lack physical justification, and the demonstration of stability of extrapolations on this basis may be of limited persuasive power.

(ii) Two methods of surface roughness analysis are mentioned in Ref. [22]. One was based on visual inspection of the original surface of a copper trap with respect to welds and oil coating at room temperature. Welds extending into the trap interior will likely represent macroscopic imperfections occupying a small fraction of the total surface. They should modify quasistationary orbits (that are confined to a limited phase space for a long time) but not preclude their existence [23]. A liquid oil coating of thickness $\geqslant 10$ μm, as estimated for the actual experiment will definitely even out any short-range micro-roughness components that could give rise to isotropic scattering. The result of surface smoothing will be the type of "soft roughness" emphasized in Sec. VIII of the article. Due to the small amplitudes of relevant roughness contributions a visual inspection may not reveal the difference.

The second method of roughness analysis mentioned in Ref. [22] is based on the data of the actual UCN experiment. We have pointed out in the article that soft roughness (as opposed to dense roughness) is not excluded by the data.

Finally, we refer to the claim in the last paragraph of Ref. [22] that our simulations must be wrong since, in Fig. 6 for the simulation with $b = 2$ nm, $w = 4$ nm (thus $\alpha = 0.71$), the first counting peak does not show the reduced intensity expected for larger roughness. The criticism appears unfounded since the first counting peak, at $t \approx 2300$ s after long storage (the dotted curve), does show the expected lower intensity as compared to the two curves for "soft roughness." The depression by a factor >2 is clearly visible on the graph. The same is true for the depression of the first counting peak following short storage.

In summary, we emphasize that more than one variety of surface roughness exists and that the interpretation of experiment [3] strongly depends on the type of roughness assumed. Most of our questions were not addressed in Ref. [22], notably how the all-important "channel" was represented in simulations in terms of geometry and surface properties and how a "quasi-spherical" trap can be modeled using a cylindrical geometry [3]. Being limited to a narrow trap and excluding the "channel," our simulations are incomplete. However, they are based on a realistic roughness model and sufficient to identify uncertainties of experiment [3]. Our conclusions regarding these uncertainties remain unchanged.

ACKNOWLEDGMENTS

We acknowledge very useful discussions with B. G. Yerozolimsky, G. Müller, R. Golub, E. Korobkina, A. V.

Strelkov, and V. K. Ignatovich. We thank N. Achiwa for measuring the temperature dependence of the scattering potential for the LTF oil.

APPENDIX A: CORRELATION FUNCTIONS

Application of the Laplace operator twice in Eq. (7) yields for the Gauss model:

$$h(\delta) = \langle \kappa(\rho)\kappa(\rho+\delta)\rangle = \kappa_G^2\left(1 - \frac{\delta^2}{w^2} + \frac{\delta^4}{8w^4}\right)\exp[-\delta^2/(2w^2)] \quad \text{(A1)}$$

with mean-square curvature

$$\kappa_G^2 = h(0) = \frac{\alpha^2}{w^2} = \frac{2b^2}{w^4}.$$

Using properties of the modified Bessel functions K_n (with $n = 0, 1, 2\ldots$) we obtain for the K_0 model

$$h(\delta) = \kappa_K^2 \frac{Q(z)}{Q(t)} \quad \text{(A2)}$$

with

$$z = \left[\left(\delta^2 + \delta_0^2\right)/(2w^2)\right]^{1/2}; \quad t = \delta_0/(w\sqrt{2})$$
$$Q(z) = 8\frac{K_2(z)}{z^2} - \frac{\delta^2}{\delta^2+\delta_0^2}\left[8\frac{K_3(z)}{z} - \frac{\delta^2}{\delta^2+\delta_0^2}K_4(z)\right] \quad \text{(A3)}$$

and

$$\kappa_K^2 = h(0) = \frac{1}{8}\frac{\alpha^2}{w^2}\left[\frac{K_3(t)}{K_1(t)} - 1\right] = 2.103\alpha^2/w^2. \quad \text{(A4)}$$

The expressions for the mean-squared curvature hold for the choice $t = 0.7709$, for which the two models have identical mean-squared slope α^2. This value of t is the solution of $K_2(t) = 5K_0(t)$.

APPENDIX B: GREEN'S FUNCTION FOR A FLAT SURFACE

Equation (10) describes the wave, with wave number k, generated at point $\mathbf{r} = (\boldsymbol{\rho}, z)$ by a point source at $\mathbf{r}' = (\boldsymbol{\rho}', z')$ near the surface $z = 0$ of a semi-infinite slab of material with scattering potential $k_c^2/4\pi$. The solution may be represented by a Fourier expansion in terms of in-plane waves $\exp(i\mathbf{k}_\parallel \cdot \boldsymbol{\rho})$ as [17]

$$G(\boldsymbol{\rho}, z|\boldsymbol{\rho}', z') = \frac{1}{(2\pi)^2}\int d^2\mathbf{k}_\parallel e^{i\mathbf{k}_\parallel\cdot(\boldsymbol{\rho}-\boldsymbol{\rho}')}g(z|z'). \quad \text{(B1)}$$

The one-dimensional Green's function for k_z satisfies the equation

$$\frac{d^2g(z|z')}{dz^2} + K_z^2(z)g(z|z') = -4\pi\delta(z-z'), \quad \text{(B2)}$$

where the wave number component perpendicular to the wall is $k_z = (k^2 - k_\parallel^2)^{1/2}$, and $K_z = k_z$ in vacuum and $K_z = k_z' = (k_z^2 - k_c^2)^{1/2}$ inside the medium. For UCN with $k^2 < k_{c0}^2$, $k_z' = i\kappa = i(k_c^2 - k_z^2)^{1/2}$ is imaginary apart from a very small real part due to the loss contribution $i\eta$ in $k_c^2 = k_{c0}^2(1 - i\eta)$. The solution of (B2) for outgoing plane waves can be written for $z > z', z > 0$:

$$g(z|z') = \frac{4\pi i}{k_z + i\kappa}e^{ik_z z}e^{\kappa z'} \cong \frac{4\pi i}{k_z + i\kappa}e^{ik_z z}(1 + \kappa z') \quad \text{(B3)}$$

and for $z < z', z < 0$:

$$g(z|z') = \frac{2\pi}{\kappa}e^{\kappa z}(e^{-\kappa z'} - Re^{\kappa z'}) \cong \frac{4\pi i}{k_z + i\kappa}e^{\kappa z}(1 + ik_z z') \quad \text{(B4)}$$

with $R = (k_z - i\kappa)/(k_z + i\kappa)$.

Both (B3) and (B4) were derived assuming $z' < 0$. The two-term approximations in (B3) and (B4) are valid for "microroughness," where $k_{c0}b \ll 1$, and they hold for positive or negative values of z' within the rough layer. This is a direct consequence of the continuity of ψ and $d\psi/dz$ at the interface. We note that the first two expansion terms are sufficient for a full description of UCN interaction with a rough wall up to terms quadratic in the roughness amplitude b.

The same kind of approximation can be made for the plane-surface wave $\psi_0(\mathbf{r}')$ in the integral of Eq. (9). Thus, using (B3) the z' integral in (9) from $z' = 0$ up to the roughness amplitude $\xi(\boldsymbol{\rho}')$ across the rough layer is proportional to $\xi + (\kappa + \kappa_i)\xi^2/2$, where $\kappa_i = (k_c^2 - k^2\cos^2\theta_i)^{1/2}$. The full Fourier expansion (B1) is needed in (9) in second-order perturbation where the first-order perturbation $\psi_1^{(1)}(\mathbf{r})$ obtained for $z \approx 0$ in (9) is subsequently inserted in the integral with ψ_0 replaced by $\psi_1^{(1)}$ to obtain $\psi_1^{(2)}(\mathbf{r})$. For flux calculations, we need the far field expressions for $G(\boldsymbol{\rho}, z|\boldsymbol{\rho}', z')$ for $z > 0$. Using the two-term approximation for its z' dependence [the last bracket in (B3)], Eq. (15) of Ref. [4] reads

$$G(\mathbf{r}|\boldsymbol{\rho}', z') \cong \frac{2k_z}{k_z + i\kappa}\frac{e^{ikr}}{r}e^{-i\mathbf{k}_\parallel\cdot\boldsymbol{\rho}'}(1 + \kappa z'). \quad \text{(B5)}$$

APPENDIX C: PERTURBATION CALCULATION UP TO SECOND ORDER

Derivation of the results listed in Sec. IV is lengthy and we will only summarize a few crucial steps, using the same symbols as in the text.

(i) Integrations over $\boldsymbol{\rho}$:
By definition of $\xi(\boldsymbol{\rho})$:

$$\int \xi(\boldsymbol{\rho})d^2\boldsymbol{\rho} = 0$$
$$\int \xi^2(\boldsymbol{\rho})d^2\boldsymbol{\rho} = A\langle\xi^2\rangle = Ab^2 \quad \text{(C1)}$$

By definition (1):

$$\int \xi(\boldsymbol{\rho})\xi(\boldsymbol{\rho}+\boldsymbol{\delta})d^2\boldsymbol{\rho} = Af(\boldsymbol{\delta}) = Af(\delta) \quad \text{(C2)}$$

By definition (15):

$$\iint \xi(\boldsymbol{\rho})\xi(\boldsymbol{\rho}')e^{i\mathbf{q}\cdot(\boldsymbol{\rho}-\boldsymbol{\rho}')}d^2\boldsymbol{\rho}d^2\boldsymbol{\rho}' = A\int f(\delta)e^{i\mathbf{q}\cdot\boldsymbol{\delta}}d^2\boldsymbol{\delta} = (2\pi)^2AF(\mathbf{q}) = (2\pi)^2AF(q) \quad \text{(C3)}$$

(ii) UCN flux:
Incoming flux for velocity $v_{\mathrm{UCN}} = \frac{\hbar k}{m}$ (with $m =$ neutron mass):

$$\Phi_{\mathrm{in}} = A v_{\mathrm{UCN}} \cos\theta_i \tag{C4}$$

Outgoing flux into solid angle $d\Omega$:

$$d\Phi_{\mathrm{out}} = v_{\mathrm{UCN}} |\psi_{\mathrm{out}}|^2 r^2 d\Omega \tag{C5}$$

For the specular beam at angle Ω_r $(\theta = \theta_i, \varphi = 0)$

$$\psi_r \sim e^{i\mathbf{k}_r\cdot\mathbf{r}} = e^{ikz\cos\theta_i} e^{ikx\sin\theta_i}$$

we can use the plane wave expansion in spherical harmonics [18] for large distance r:

$$e^{i\mathbf{k}_r\cdot\mathbf{r}} \to \frac{2\pi}{ik}\frac{e^{ikr}}{r}\sum_{l=0}^{\infty}\sum_{m=-l}^{+l} Y_l^{m*}(\theta_i,0)Y_l^m(\theta,\varphi)$$
$$= \frac{2\pi}{ik}\frac{e^{ikr}}{r}\delta(\Omega-\Omega_r). \tag{C6}$$

This allows simple integration of the interference integrals.

(iii) Loss terms: On each step the terms containing the loss coefficient η are developed to first order in η. For instance, for k_z not too close to k_{c0}:

$$\kappa = \sqrt{k_c^2 - k_z^2} \cong \kappa_0 - \frac{i\eta}{2}\frac{k_{c0}^2}{\kappa_0} \tag{C7}$$

with $k_c^2 = k_{c0}^2(1 - i\eta)$ and $\kappa_0 = \sqrt{k_{c0}^2 - k_z^2}$

APPENDIX D: INTEGRATIONS IN q SPACE

Using the transformation $d\Omega\cos\theta = \nu d\nu d\psi$ and the relationship

$$\cos^2\theta = 1 - (s_i - \nu)^2 - 4\nu s_i \sin^2(\psi/2),$$

the integrations over ψ in (17)–(20) can be performed analytically. The integrations run from 0 to ψ_u, where

$$\sin\frac{\psi_u}{2} = \begin{cases} 1; & \text{for} \quad \nu \leqslant 1 - s \\ \sqrt{\frac{1-(\nu-s_i)^2}{4\nu s_i}}; & \text{for} \quad 1 + s_i \geqslant \nu \geqslant 1 - s_i. \end{cases} \tag{D1}$$

Since the ψ integrals needed in (18) to (20) do not appear to be readily available from tables or Web sites we list two results:

$$\int_0^{\psi_u} \cos\theta d\psi = \begin{cases} 2v_-^{1/2}\mathbf{E}(m_1); & \nu \leqslant 1 - s_i \\ 2\sigma^{1/2}\mathbf{E}\left(m_1^{-1}\right) + 2v_+\sigma^{-1/2}\mathbf{K}\left(m_1^{-1}\right); & 1 + s_i \geqslant \nu \geqslant 1 - s_i \end{cases} \tag{D2}$$

and

$$\int_0^{\psi_u} \frac{2\zeta^2\cos^2\theta - 1}{\sqrt{1-\zeta^2\cos^2\theta}} d\psi = \begin{cases} 2u_+^{-1/2}\mathbf{K}(m_2) - 4u_+^{1/2}\mathbf{E}(m_2); & \nu \leqslant 1 - s_i \\ 2u_+^{-1/2}F(\omega_1|m_2) - 4u_+^{1/2}E(\omega_1|m_2) + 4\zeta^2(-v_-v_+)^{1/2}; & 1 + s_i \geqslant \nu \geqslant 1 - s_i, \end{cases} \tag{D3}$$

where [19]

$$F(\omega|m) = \int_0^{\omega} (1 - m\sin^2\beta)^{-1/2} d\beta \tag{D4}$$

is the incomplete elliptic integral of the first kind,

$$E(\omega|m) = \int_0^{\omega} (1 - m\sin^2\beta)^{1/2} d\beta \tag{D5}$$

is the incomplete integral of the second kind, and $\mathbf{K}(m) = F(\frac{\pi}{2}|m)$ and $\mathbf{E}(m) = E(\frac{\pi}{2}|m)$ are the corresponding complete elliptic integrals of the first and second kinds, respectively. The arguments in (D2) and (D3) are $\zeta = \frac{k}{k_{c0}}$; $v_\pm = 1 - (\nu \pm s_i)^2$; $u_\pm = 1 - \zeta^2 v_\pm$; $\sigma = 4\nu s_i$; $m_1 = \frac{\sigma}{v_-}$; $m_2 = \frac{\sigma\zeta^2}{u_+}$; $\sin\omega_1 = (\frac{v_- u_+}{\sigma})^{1/2}$.

Compared to numerical double integration, the use of these readily available functions in one of the integrals as well as tabulation of the numerical results for use in simulations is of enormous benefit.

APPENDIX E: MACROSCOPIC LIMIT

In the geometrical optics model, reflection is considered as an incoherent superposition of rays reflected at each speck of a fairly smooth surface ($\alpha \ll 1$) as if it were a plane inclined at the local slope. The analysis is based on a slope distribution function $p(\chi)$ that has to be postulated independently of the correlation function $g(\delta)$. For instance, $p(\chi)$ does not have to be Gaussian if $g(\delta)$ has been chosen Gaussian. If the simplest Gaussian is chosen, as in Ref. [4], it is of the form

$$p(\chi) = p(|\boldsymbol{\chi}|) = 2\pi\chi p(\boldsymbol{\chi}) = \frac{2\chi}{\alpha^2} e^{-\chi^2/\alpha^2}, \tag{E1}$$

which is normalized and has the correct second moment $\langle\chi^2\rangle = \alpha^2$ The ambiguity is more obvious for the K_0 model. Requiring that $p(\chi)$ should be a monotonic, bounded function, exhibit an asymptotic K-Bessel function behavior, and, for convenience, be amenable to analytic analysis, we can choose

$$p(\boldsymbol{\chi}) = A\frac{K_\nu(Z)}{Z^\nu}, \tag{E2}$$

where $Z = \frac{1}{\alpha}(\chi^2 + \beta^2)^{1/2}$. For any $\nu > 3/4$, values of A and β can be determined analytically [20] such as to satisfy the normalization and second moment criteria. For $\nu = 1$: $\beta = \upsilon\alpha$ and $A = [\pi\alpha K_0(\upsilon)]^{-1}$ where $\upsilon = 0.1657$ is the solution to $K_0(\upsilon) = 2\upsilon K_1(\upsilon)$. For small values of α, the K model, as compared with the Gauss model, describes a surface with

higher probability of large slope ($\chi \gg \alpha$) at the expense of areas with a very small slope.

In the macroscopic-roughness model the probability of scattering (local reflection) from Ω_i to Ω, i.e., from angles $(\theta_i, 0)$ to (θ, φ), at suitably oriented surface elements is

$$\frac{dP}{d\Omega} d\Omega = p(\boldsymbol{\chi}) d^2\boldsymbol{\chi} = p(\boldsymbol{\chi}) d\chi_x d\chi_y. \tag{E3}$$

The mapping $\boldsymbol{\chi} \to \Omega$ involves the local polar angle of incidence, θ', where

$$c' = \cos\theta' = \left[c_+^2 \cos^2\left(\frac{\varphi}{2}\right) + c_-^2 \sin^2\left(\frac{\varphi}{2}\right)\right]^{1/2} \tag{E4}$$

with $c_\pm = \cos[(\theta \pm \theta_i)/2]$. We obtain

$$d\Omega = \frac{4c_+^3 c_-^3}{c'^2} d^2\boldsymbol{\chi}. \tag{E5}$$

Inserting (E5) and (E1) into (E3) gives the scattering distribution. For the Gaussian model,

$$I_{sc}(\Omega_i \to \Omega) = \frac{dP}{d\Omega} = \frac{1}{4\pi\alpha^2} \frac{c'^2}{c_+^3 c_-^3} \exp\left[-\frac{q^2}{(2\alpha k c_+ c_-)^2}\right], \tag{E6}$$

where the in-plane momentum transfer q is given in (11).

Equation (E6) is consistent with the limiting case analyzed in Ref. [4] (Eq. (26) of Ref. [4]) and it closely resembles the micro-roughness result (14) for $I_{(11)}$ (for $\eta = 0$). It exhibits a similar width of scattering distribution around the regular reflection angle $(\theta_i, 0)$ but no exactly specular intensity. Local angle (θ') dependent loss could be incorporated in the form $\mu_0(\theta')$ as for a plane surface, but the result differs from the micro-roughness result (25) for $\alpha \ll 1$. The angle-dependent second term in the curly bracket of (25), $-\frac{s_i^2}{2c_i^2}\frac{2+\zeta^2 c_i^2}{1-\zeta^2 c_i^2}$, changes significantly to $-\frac{3}{2}\frac{\zeta^2 s_i^2}{1-\zeta^2 c_i^2}$. Both terms are valid for $\frac{\pi}{2} - \theta_i \gg \alpha$.

Expression (E6) and similar expressions for non-Gaussian models are symmetric in Ω_i and Ω, thus do not satisfy the detailed balance requirement discussed in Sec. VI, and indeed give rise to loss of isotropy in computer simulations. Moreover, (E6) is catastrophically inadequate for glancing-angle incidence ($\theta_i \to \pi/2$) due to shadowing and multiple reflection within a rough surface as discussed in Sec. VI. Although this angular range is small, it makes a large contribution to the mean value for isotropic incident UCN flux and cannot be neglected. For large mean surface slope α no meaningful transition to ray optics appears possible. Unless the amplitude b also increases, surface patches of any specific orientation will be too small to be represented by an infinite reflecting plane.

[1] P. Croce, L. Névot, and B. Pardo, C. R. Acad. Sci. Paris **274**, 803 (1972); **274**, 855 (1972).

[2] C. Amsler *et al.* (Particle Data Group), Phys. Lett. B **667**, 1 (2008).

[3] A. Serebrov *et al.*, Phys. Lett. B **605**, 72 (2005); and extended version of PNPI preprint 2564 (2004) [our references relate to the latter version]; also in A. P. Serebrov *et al.*, Phys. Rev. C **78**, 035505 (2008).

[4] A. Steyerl, Z. Phys. **254**, 169 (1972).

[5] S. K. Sinha, E. B. Sirota, S. Garoff, and H. B. Stanley, Phys. Rev. B **38**, 2297 (1988).

[6] A. Steyerl, S. S. Malik, and L. R. Iyengar, Physica B **173**, 47 (1991).

[7] V. K. Ignatovich, *The Physics of Ultracold Neutrons* (Clarendon, Oxford, 1990), especially Appendix 6.10, and personal communication.

[8] A. Steyerl, in *Neutron Physics*, Springer Tracts in Modern Physics (Springer-Verlag, Berlin, 1977), Vol. 80, 57–127.

[9] R. Golub, D. Richardson, and S. K. Lamoreaux, *Ultra-Cold Neutrons* (Hilger, Bristol, 1991).

[10] A. Steyerl, B. G. Yerozolimsky *et al.*, Eur. Phys. J. B **28**, 299 (2002).

[11] Using a distorted-wave Born approximation, the expression $\exp(-4b^2 k k' \cos\theta_i \cos\theta_i')$ was obtained in Refs. [1] and [5], where the primed quantities refer to the quantities inside the refractive medium. This modification is clearly inapplicable within the total reflection range, where $k' \cos\theta_i'$ is imaginary (approaching zero at the edge).

[12] A. V. Stepanov, Teor. Mat. Fiz. **22**, 425 (1975).

[13] F. Achison *et al.*, Nucl. Instrum. Methods A **552**, 513 (2005).

[14] I. Berceanu and V. K. Ignatovich, Vacuum **23**, 441 (1973).

[15] M. Brown, R. Golub, and J. M. Pendlebury, Vacuum **25**, 61 (1975).

[16] P. Geltenbort *et al.* [http://surface.phys.uri.edu/Publications-Steyerl/list/n-lifetime.2003.pdf].

[17] P. M. Morse and H. Feshbach, *Methods of Theoretical Physics* (McGraw–Hill, New York, 1953), Chap. 7.

[18] A. Messiah *Quantum Mechanics* (Wiley, New York, 1961), Vol. 1, Appendix B.10.

[19] M. Abramowitz and I. A. Stegun, *Handbook of Mathematical Functions* (Dover, New York, 1970).

[20] I. S. Gradshteyn and I. M. Ryzhik, *Table of Integrals, Series, and Products* (Academic Press, New York, 1980), Eq. 6.596.7.

[21] A. Steyerl, *Systematics in Neutron Lifetime Experiments*, Res. Opp. with UCN in the US, Santa Fe, 2009 [http://neutron.physics.ncsu.edu/UCN_Workshop_09/Steyerl_SantaFe_2009.pdf].

[22] A. Serebrov, A. Fomin, and V. Varlamov, arXiv:1001.3210.

[23] J. D. Bowman, *Neutron Lifetime Measurements: Some Problems with Gravo-Magneto Traps*, Res. Opp. with UCN in the US, Santa Fe, 2009 [http://neutron.physics.ncsu.edu/UCN_Workshop_09/Bowman_SantaFe_2009.pdf].